Combining Multi-Task Learning and Multi-Channel Variational Auto-Encoders to Exploit Datasets with Missing Observations -Application to Multi-Modal Neuroimaging Studies in Dementia

Luigi Antelmi, Nicholas Ayache, Philippe Robert, Federica Ribaldi, Valentina Garibotto, Giovanni B Frisoni, Marco Lorenzi

Combining Multi-Task Learning and Multi-Channel Variational Auto-Encoders to Exploit Datasets with Missing Observations - Application to Multi-Modal Neuroimaging Studies in Dementia

Luigi Antelmi[1,*], Nicholas Ayache[1], Philippe Robert[2,3], Federica Ribaldi[4,5,6,7], Valentina Garibotto[8,9], Giovanni B. Frisoni[6,7], Marco Lorenzi[1], for the Alzheimer's Disease Neuroimaging Initiative[**]

Abstract

The joint modeling of neuroimaging data across multiple datasets requires to consistently analyze high-dimensional and heterogeneous information in presence of often non-overlapping sets of views across data samples (e.g. imaging data, clinical scores, biological measurements). This analysis is associated with the problem of missing information across datasets, which can take place in two forms: missing at random (MAR), when the absence of a view is unpredictable and does not depend on the dataset (e.g. due to data corruption); missing not at random (MNAR), when a specific view is absent by design for a specific dataset. In order to take advantage of the increased variability and sample size when pooling together observations from many cohorts, and at the same time cope with the ubiquitous problem of missing information, we propose here a multi-task generative latent-variable model where the common variability across datasets stems from the estimation of a shared latent representation across views. Our formulation allows to retrieve a consistent latent representation common to all views and datasets, even in the presence of missing information. Simulations on synthetic data show that our method is able to identify a common latent representation of multi-view datasets, even when the compatibility across datasets is minimal. When jointly analyzing multi-modal neuroimaging and clinical data from real independent dementia studies, our model is able to mitigate the absence of modalities without having to discard any available information. Moreover, the common latent representation inferred with our model can be used to define robust classifiers gathering the combined information across different datasets. To conclude, both on synthetic and real data experiments, our model compared favorably to state of the art benchmark methods, providing a more powerful exploitation of multi-modal observations with missing views. Code is publicly available at `https://gitlab.inria.fr/epione_ML/mcvae`.

1. Introduction

Because of the inherent complexity of biomedical data and diseases, researchers are required to integrate data across different studies to increase the sample size and obtain better models (Le Sueur et al., 2020). When developing integrative models, researchers have to face with multiple concurrent challenges, such as the ones related to datasets interoperability (Tognin et al., 2020), data heterogeneity (Buch and Liston, 2020), and data missingness (Golriz Khatami et al., 2020). Emblematic is the case of integrative modeling when datasets come from multi-centric studies in cognitive and neurological disorders, such as in Alzheimer's Disease (AD). Here the datasets interoperability is hampered by the existence of different protocols between studies. Because of this, methods whose modeling task are specifically designed on one dataset cannot be directly applied to another one. Furthermore, at the level of each single dataset, researchers face the challenge of modeling heterogeneous data, such as multiple imaging modalities, clinical scores and biological measurements. Each of these sources of information represents an important and independent "*view*" on the disease or phenomena under investigation. Efforts to model multi-view data are increasing in the recent biomedical literature (Vieira et al., 2020; Venugopalan et al., 2021), where the objective ranges from predicting clinical outcomes (Chen et al., 2019; Abi Nader et al., 2020; Tabarestani et al., 2020) to synthesizing new modalities (Wei et al., 2019, 2020; Zhou et al., 2020). The key concept of a shared information space between views is widespread in the literature for

[*]Corresponding author: luigi.antelmi@inria.fr

[**]Data used in preparation of this article were obtained from the Alzheimer's Disease Neuroimaging Initiative (ADNI) database (http://adni.loni.usc.edu). As such, the investigators within the ADNI contributed to the design and implementation of ADNI and/or provided data but did not participate in analysis or writing of this report. A complete listing of ADNI investigators can be found at http://adni.loni.usc.edu/wp-content/uploads/how_to_apply/ADNI_Acknowledgement_List.pdf

[1]University of Côte d'Azur, Inria, Epione Project-Team, France.

[2]University of Côte d'Azur, CoBTeK, France.

[3]Centre Mémoire, CHU of Nice, France

[4]Laboratory of Alzheimer's Neuroimaging and Epidemiology (LANE), Saint John of God Clinical Research Centre, Brescia, Italy.

[5]Department of Molecular and Translational Medicine, University of Brescia, Brescia, Italy.

[6]Laboratory of Neuroimaging of Aging (LANVIE), University of Geneva, Geneva, Switzerland.

[7]Memory Clinic, Geneva University Hospitals, Geneva, Switzerland.

[8]Laboratory of Neuroimaging and Innovative Molecular Tracers (NIMTlab), Geneva University Neurocenter and Faculty of Medicine, University of Geneva, Geneva, Switzerland.

[9]Division of Nuclear Medicine and Molecular Imaging, Diagnostic Department, Geneva University Hospitals, Geneva, Switzerland.

the joint model of multi-view data. This is the case for well established multivariate linear methods such as Canonical Correlation Analysis (CCA), Partial Least Squares (PLS), Independent Component Analysis (ICA), which are some of the most popular methods for multivariate analyses on imaging data, as documented in a multitude of works from the state of the art (see Liu and Calhoun (2014) for a general review). While these studies essentially focus on the general problem of multivariate association modeling, multi-view methods specifically tailored to medical imaging tasks, such as image registration and segmentation have been proposed in parallel. For example, in Qin et al. (2019) the authors propose a registration method for aligning intra-subject multi-view images. Although limited to a two images registration setting, in this work views are projected into a common latent space. The proposed registration approach is then built on the latent code and on an image-to-image translation approach. Chartsias et al. (2021) propose a segmentation method based on the learning of information presented jointly in complementary imaging views. From the different inputs views, anatomical factors are encoded into a common latent space and fused to extract more accurate segmentation masks. In Yang et al. (2020) a cross-modality segmentation pipeline is built around a similar concept. In all the works cited so far, the problem of missing data, specifically of missing views during training of multi-view methods, is generally not addressed nor considered. Still, this is a very common problem when joint modeling multiple datasets, especially in neuroimaging research. At the level of the single dataset, views can be missing at random (MAR) for some subjects. Typically, as fitting multi-view models requires to establish correspondences between views, observations with at least one missing view are generally discarded, yielding to potentially severe loss of available information. To mitigate this problem, imputation methods can be applied to infer missing views, by modeling the relationship across views from complete observations. The loss of information is exacerbated when considering multiple datasets altogether. Indeed, according to the cohort study design, there may be views which are specifically absent for a given dataset, hence missing not at random (MNAR). This potential mismatch across datasets hampers their interoperability, and prevents the gathering of all the available observations into a single, robust and generalizable joint model accounting for the global data variability. This challenge is typically addressed in machine learning by the field of Multi Task Learning (MTL). To address this issue, MTL aims at improving the model interoperative capabilities by exploiting the information extracted from multiple datasets. In MTL each task is usually associated to the modeling of a specific dataset and its views only, when the main idea consists is sharing across datasets the parameters learned through each modeling task (Caruana, 1998; Dorado-Moreno et al., 2020). As an example of MTL, in model-agnostic meta-learning (MAML) (Finn et al., 2017) the training of a model on a variety of learning tasks enforces the generalization on new datasets after few fine tuning iterations. In the context of data assimilation, MTL is usually achieved with specific output layers for every task, and by including a shared latent representation for all of them (Dorado-Moreno et al., 2020). This modeling rationale is at the basis of recent MTL based approaches to heterogeneous data assimilation (Wu and Goodman, 2018; Shi et al., 2019), especially in medical imaging approaches. For example, in Zhou et al. (2019), the authors propose a staged deep learning framework for dementia diagnosis classification, able to jointly exploit multi-view data (MRI, PET, and genetic data in this case). Their approach, where at each stage the model learns feature representations for different combinations of views, solves elegantly the problem of missing data. Although inspiring for their use of the maximum number of available data samples at each stage, the combinatorial nature of their framework makes it in practice applicable only for datasets with very few available views. For example, when considering 3 views, this approach requires to learn 7 networks. With 4 views, the number of networks that need to be trained, considering all the possible couples, triplets and quadruplets of views amounts to 4845; while with 5 views it exceeds 10^{32}. Moreover, this framework is currently designed for classification tasks only, excluding the possibility of modality-to-modality prediction. With the *EmbraceNet* of Choi and Lee (2019) the problem of missing data is managed by zero-filling the missing input views and by the application of a specific dropout technique where multinomial samples are used to assign partitions of the latent space to specific views. As there are latent features that are randomly discarded even when the correspondent view is not missing, this represents still a loss of information. Similarly as for the previous work, the proposed framework is currently applicable in classification tasks only. Dropout is at the basis of the *Denoising Autoencoder*, as developed by Gondara and Wang (2018). Here an overcomplete deep autoencoder maps input views to a higher dimensional space. The initial dropout layer induces random corruption in the input views, making the model robust to missing data. This framework is currently applicable in feature prediction tasks only.

The common underlying assumption of these approaches consists in the existence of a proper transformation into a common latent code for the solution of multiple tasks, whether classification or feature prediction. Based on this general assumption, the Multi-Channel Variational Autoencoder (MCVAE) (Antelmi et al., 2019) is a recent analysis method allowing the identification of a common latent representation for different views belonging to a single dataset (Fig. 1). MCVAE extends currently available approaches to account for non-linear transformations from the data to the latent space, while it can be adapted to multiple tasks, including data reconstruction and classification. In spite of the high modeling flexibility, the extension of this method to the analysis of multiple datasets is currently challenging. Training the MCVAE in a multi-dataset context is indeed possible with some limitations: 1) after having discarded observations with missing views; 2) when at train time all the observations are compatible in terms of available views.

To overcome these limitations, in this work we investigate an extension of MCVAE to simultaneously learn from multiple datasets, even in the presence of non compatible views between datasets, and missing views within datasets. While our formulation naturally extends the original MCVAE approach, to the

best of our knowledge no systematic investigation of this approach for the modeling of multi-view and multi-dataset neuroimaging data has been proposed so far. Our extension is built upon the following steps: 1) defining tasks across datasets based on the identification of data subsets presenting compatible views, 2) stacking multiple instances of the MCVAE, where each instance models a specific task, 3) sharing the models parameters of common views between modeling tasks. Thanks to these actions, the framework here proposed allows to learn a joint model for all the subjects without discarding any information (Fig. 2). The common views between tasks act as a bridge and enable the information to flow through all the other views, while, in the training phase, tasks lacking a particular view will simply not contribute to the learning of those view-specific parameters. All the tasks will nevertheless benefit from the parameters they didn't contribute to learn, for the prediction of their missing views. The proposed variational formulation for computing approximate posterior distributions of the latent variables allows fast and scalable training. Being dataset agnostic, our method allows to integrate all the available data into a joint model, gathering all the available information from multiple datasets at the same time.

The rest of this paper is structured as follow. In § 2 we present the mathematical derivation of the classical MCVAE model that will be used to derive the proposed framework. In § 3.1 we show an illustrative application for the joint modeling of MRI and PET images when some modalities are missing in the training phase. In § 3.2, experiments on synthetic data show that the prediction error of missing views is competitive with respect to the one obtained with state of the art imputation methods. In § 3.3, experiments on real data from independent multi-modal neuroimaging datasets show that our model generalizes better than dataset-specific models, in both the cases of data reconstruction and diagnosis classification. Lastly we discuss our results and conclude our work with summary remarks.

2. Method

In this section we recall the theoretical framework of the *Multi-Channel Variational Autoencoder* (MCVAE) developed in our previous work (Antelmi et al., 2019), which we now extend to tackle the problem of missing data integration. In § 2.1 and § 2.2 we introduce our framework, the *Multi-Task MCVAE* (MT-MCVAE), and derive the model in presence of missing data. In § 2.3 we propose the new optimization scheme allowing to account for observations with partially missing views. In § 2.4 we emphasize the differences between the MCVAE and our current approach. In § 2.5 we briefly recall the main parametric functions adopted later in our experiments with missing data. Code developed in Pytorch (Paszke et al., 2019) is publicly available at `https://gitlab.inria.fr/epione_ML/mcvae`.

2.1. Generative Model

Let $\mathcal{D} = \{D_d\}_{d=1}^{D}$ be a collection of D independent datasets, where each dataset $D_d = \{\mathbf{x}_{d,n}\}_{n=1}^{N_d}$ is composed by N_d independent data-points (*e.g.,* subjects in the case of medical imaging datasets). Every dataset D_d is associated with a total number of V_d available views (*e.g.,* sets of clinical scores and imaging derived phenotypes extracted from multiple imaging modalities), and we assume that each data-point $\mathbf{x}_{d,n} = \{\mathbf{x}_{d,n,v}\}_{v=1}^{V_{d,n}}$ is composed by $V_{d,n}$ views, where $V_{d,n} \leq V_d$. With the latest inequality we account for data-points with an arbitrary number of missing views.

For each view $\mathbf{x}_{d,n,v}$ we rely on the following generative latent variable model:

$$\begin{aligned} &\mathbf{z}_{d,n} \sim p(\mathbf{z}), \\ &\mathbf{x}_{d,n,v} \sim p(\mathbf{x}_{d,n,v}|\mathbf{z}_{d,n}, \boldsymbol{\theta}_v), \qquad \text{for } v \text{ in } 1 \dots V_{d,n} \leq V_d, \end{aligned} \tag{1}$$

where $p(\mathbf{z})$ is a prior distribution for the latent variable $\mathbf{z}_{d,n}$ commonly shared by the $V_{d,n}$ views, and where the likelihood functions $p(\mathbf{x}_{d,n,v}|\mathbf{z}_{d,n}, \boldsymbol{\theta}_v)$ belong to a family of distributions parametrized by $\boldsymbol{\theta}_v$, which represents the view-specific generative parameters shared among all datasets.

2.2. Inference Model

The exact solution to the inference problem is given by the posterior $p\left(\mathbf{z}|\{\mathbf{x}_{d,n,v}, \boldsymbol{\theta}_v\}_{v=1}^{V_{d,n}}\right)$, that is not generally computable analytically. Following Antelmi et al. (2019), we can nevertheless look for its approximation through *Variational Inference* (Blei et al., 2017), applied in our specific context of missing data.

The variational approximations $q(\mathbf{z}|\mathbf{x}_{d,n,w}, \boldsymbol{\phi}_w)$, where $\boldsymbol{\phi}_w$ represents the view-specific variational parameters shared among all datasets, are such that:

$$\ln p(\mathbf{x}_{d,n,v}|\boldsymbol{\theta}_v) \geq \mathcal{L}_v^{(\mathbf{x}_{d,n})} = \frac{1}{V_{d,n}} \sum_{w=1}^{V_{d,n}} \mathcal{L}_{w\to v}^{(\mathbf{x}_{d,n})}, \tag{2}$$

where:

$$\mathcal{L}_{w\to v}^{(\mathbf{x}_{d,n})} = \mathbb{E}_{q_{d,n,w}(\mathbf{z})}\left[\ln p(\mathbf{x}_{d,n,v}|\mathbf{z}, \boldsymbol{\theta}_v)\right] - \mathcal{D}_{\mathrm{KL}}\left(q_{d,n,w}(\mathbf{z})\|p(\mathbf{z})\right) \tag{3}$$

is the lower bound associated to the data-point $\mathbf{x}_{d,n}$ when its view v is predicted from its view w. In Fig. 1 we sketch the model structure induced by Eq. (3). The complete derivation of Eq. (2) is detailed in the *Supplementary Material* section of this work.

2.3. Optimization

Assuming independent observations, the marginal log-likelihood in the left hand side of Eq. (2) can be summed up over all the datasets, data-points, and views. As a consequence, inference on the model generative parameters $\boldsymbol{\theta} = \{\boldsymbol{\theta}_v\}$ and variational parameters $\boldsymbol{\phi} = \{\boldsymbol{\phi}_w\}$ can be achieved by solving the maximization problem:

$$\begin{aligned} \hat{\boldsymbol{\theta}}, \hat{\boldsymbol{\phi}} &= \arg\max_{\boldsymbol{\theta},\boldsymbol{\phi}} \sum_{d,n,v} \mathcal{L}_v^{(\mathbf{x}_{d,n})} \\ &= \arg\max_{\boldsymbol{\theta},\boldsymbol{\phi}} \sum_{d,n,v} \frac{1}{V_{d,n}} \sum_{w=1}^{V_{d,n}} \mathcal{L}_{w\to v}^{(\mathbf{x}_{d,n})}. \end{aligned} \tag{4}$$

We implemented Algorithm 1 to solve Eq. (4). The summation

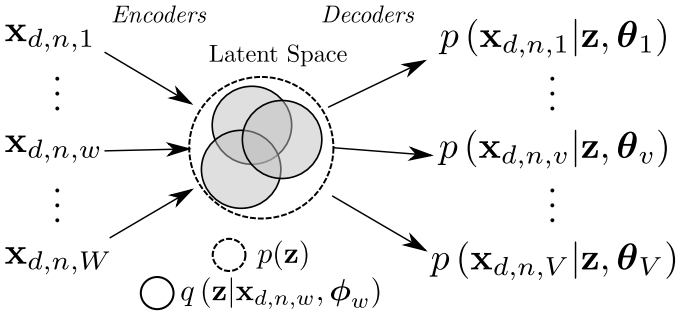

Figure 1: General variational framework for our multi-view and multi-dataset model. Compatibly with the MCVAE formulation, for every pair of views w and v there is a prediction path $w \rightarrow v$ composed by two learnable functions: the encoding distribution $q(\mathbf{z}|\mathbf{x}_{d,n,w}, \boldsymbol{\phi}_w)$ and the decoding likelihood $p(\mathbf{x}_{d,n,v}|\mathbf{z}, \boldsymbol{\theta}_v)$. Parameters $\boldsymbol{\phi}_w$ and $\boldsymbol{\theta}_v$ are optimized through Eq. (4) to maximize the likelihood of our generative model under the encoding distributions, and at the same time minimize the Kullback-Leibler distance between every encoding distribution and the prior $p(\mathbf{z})$.

Algorithm 1 Multi-view model optimization.

Require:
Set the dimensionality of $\mathbf{z}$.
Initialize the model parameters $\boldsymbol{\phi}, \boldsymbol{\theta}$.
Set the optimizer learning rate.

while $\boldsymbol{\phi}, \boldsymbol{\theta}$ not converged **do**
  Initialize the total cost:
  $\mathcal{L} \leftarrow 0$
  for every dataset $d \in D$ **do**
    for every datapoint $\mathbf{x}_{d,n}, n \in N_d$ **do**
      for every view $v \in V_{d,n}$ **do**
        Accumulate the cost of predicting v from w:
        $\mathcal{L}_v \leftarrow 0$
        for every view $w \in V_{d,n}$ **do**
          $\mathcal{L}_v \leftarrow \mathcal{L}_v + \mathcal{L}_{w \rightarrow v}^{(\mathbf{x}_{d,n})}$. See Eq. (3).
        end for
        Accumulate the average $\mathcal{L}_v$ in the total cost:
        $\mathcal{L} \leftarrow \mathcal{L} + \frac{1}{V_{d,n}} \mathcal{L}_v$.
      end for
    end for
  end for
  $\boldsymbol{\theta}, \boldsymbol{\phi} = \text{Optim}(\boldsymbol{\phi}, \boldsymbol{\theta}, \nabla_{\boldsymbol{\phi}} \mathcal{L}, \nabla_{\boldsymbol{\theta}} \mathcal{L})$. *Adam* optimizer used to maximize $\mathcal{L}$.
end while

in Eq. (4) is done for every dataset d along all the available datapoints n and their specific views v. If missing, a particular view v will be simply not accounted for that specific observation, without having to discard all the other views that can still contribute to optimize Eq. (4). We note that batching data-points with common views can speed up the computation by reducing the number of second level *for* loop iterations in Algorithm 1. The presence of at least one common view among datasets acts as a link across datasets and allows the information to flow through all the datasets to the other views. In Fig. 2 the learning scheme of our model in a simple case with four views and one common view between batches.

2.4. Comparison with VAE and MCVAE

In Tab. 1 we show how the Multi-Task framework detailed in Algorithm 1 extends the capabilities of the Multi-Channel VAE (MCVAE, Antelmi et al. (2019)), which is itself a multi-view extension of the VAE (Kingma and Welling, 2014; Rezende et al., 2014). In our former work we proposed a multi-view generative model trainable only with observation in the training set have all the available views, limited to model one dataset at a time (in the case of datasets with multiple views), after having discarded incomplete observations in that dataset. We address this limitation by allowing missing views in the training set for some observations, thanks to the adapted optimization scheme in Eq. (4). This aspect naturally extends the training paradigm of MCVAE to the more challenging scenario of multi-dataset analysis. As in the MCVAE, at test time, the trained

Table 1: The Multi-Task Multi-Channel VAE (MT-MCVAE) extends the MCVAE, which is itself an extension of the VAE.

Method	Train with missing data	Test with missing data	# views modeled
VAE	no	no	1
MCVAE	no	yes	> 1
MT-MCVAE	yes	yes	> 1

MT-MCVAE model can estimate missing views $\hat{\mathbf{x}}_{d,n,v}$ from the available ones through the formula:

$$\hat{\mathbf{x}}_{d,n,v} = \frac{1}{V_{d,n} - 1} \sum_{w=1, w \neq v}^{V_{d,n}} \mathbb{E}_{q_{d,n,w}(\mathbf{z})} \left[p(\mathbf{x}_{d,n,v}|\mathbf{z}, \boldsymbol{\theta}_v) \right], \qquad (5)$$

where the available views $\mathbf{x}_{d,n,w}$ are encoded into the distributions $q_{d,n,w}$, which are then used to predict the missing view through its decoding distribution $p(\mathbf{x}_{d,n,v}|\mathbf{z}, \boldsymbol{\theta}_v)$.

2.5. Parameterization

With the right choice of the functional form of $q(\mathbf{z}|\mathbf{x}_{d,n,w}, \boldsymbol{\phi}_w)$, $p(\mathbf{z})$, and $p(\mathbf{x}_{d,n,v}|\mathbf{z}, \boldsymbol{\theta}_v)$, the right hand side of Eq. (2) becomes amenable to computation and optimization, yielding to the maximization of the left hand side, quantity also known as the model evidence. Of course, the choice for the likelihood function $p(\mathbf{x}_{d,n,v}|\mathbf{z}, \boldsymbol{\theta}_v)$ depends on the nature of the view $\mathbf{x}_{d,n,v}$. For example it can be parametrized as a multivariate Gaussian in the case of continuous data (*i.e.,*imaging derived phenotypes), as a Bernoulli likelihood for dichotomic data, and as a Categorical likelihood for categorical data.

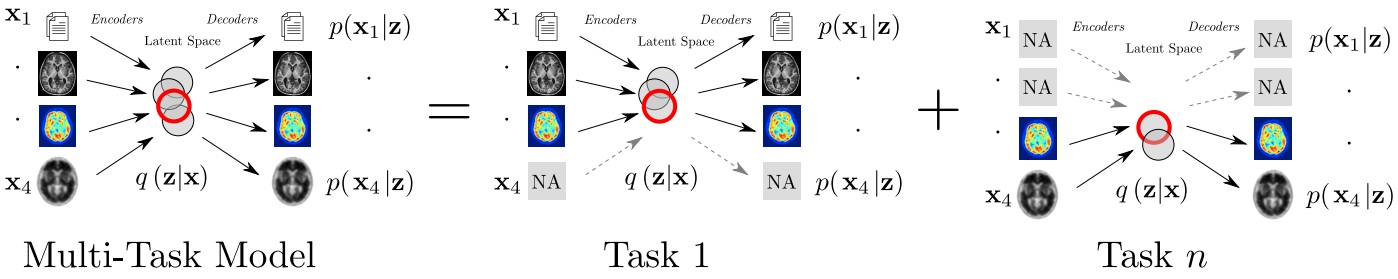

Figure 2: Simple example of a Multi-Task Model learning scheme in the presence of missing not available (NA) views. Arrows represent learnable functions used as network encoders and decoders, transforming respectively input views (*e.g.,* clinical scores, imaging derived phenotypes, ...) from the observation space to the representation space (circles) and from the representation space back to the observation space. The separability of the loss function $\mathcal{L}_v^{(\mathbf{x}_{d,n})}$ in Eq. (2) allows to group together observations into homogeneous learning tasks. For every task, functions associated to missing views (dashed gray arrows) are locally not updated by the learning algorithm. Globally, common latent representations (red circles) across pairs of tasks act as a link allowing the information to flow throughout the views.

2.5.1. Linear parameterization

In general, the prior distribution $p(\mathbf{z})$ is the multivariate Gaussian distribution $\mathcal{N}(\mathbf{0};\mathbf{I})$. The same family of distributions is also commonly used for the variational and likelihood functions, such that respectively:

$$q(\mathbf{z}|\mathbf{x}_{d,n,w},\boldsymbol{\phi}_w) = \mathcal{N}\left(\boldsymbol{\mu} = \mathbf{V}_w^{(\mu)}\mathbf{x}_{d,n,w}\,;\,\boldsymbol{\Sigma} = \mathrm{diag}\left(\mathbf{V}_w^{(\sigma)}\mathbf{x}_{d,n,w}\right)\right), \tag{6}$$

$$p(\mathbf{x}_{d,n,v}|\mathbf{z},\boldsymbol{\theta}_v) = \mathcal{N}\left(\boldsymbol{\mu} = \mathbf{G}_v^{(\mu)}\mathbf{z} \quad ;\boldsymbol{\Sigma} = \mathrm{diag}\left(\mathbf{g}_v^{(\sigma)}\right)\right), \tag{7}$$

where the moments $\boldsymbol{\mu}$ and $\boldsymbol{\Sigma}$ are obtained from linear transformations of the conditioning variables. Here, $\boldsymbol{\theta}_v = \{\mathbf{G}_v^{(\mu)}, \mathbf{g}_v^{(\sigma)}\}$ and $\boldsymbol{\phi}_w = \{\mathbf{V}_w^{(\mu)}, \mathbf{V}_w^{(\sigma)}\}$ are the parameters to be optimized. A non-linear parameterization can be used as well, for example in the form of deep neural networks.

In Antelmi et al. (2019) we also introduced the following alternative parameterization for the posterior distribution:

$$q_{d,n,w}(\mathbf{z}) = \mathcal{N}\left(\boldsymbol{\mu} = \mathbf{V}_w^{(\mu)}\mathbf{x}_{d,n,w};\boldsymbol{\Sigma} = \mathrm{diag}\left(\sqrt{\boldsymbol{\alpha}}\odot\boldsymbol{\mu}^2\right)\right), \tag{8}$$

which is known as *dropout posterior* (Kingma et al., 2015). The dropout parameter $\boldsymbol{\alpha}$ has components $\alpha_i = p_i/1-p_i$ linked to the probability p_i of dropping out the i-th latent variable component (Wang and Manning, 2013). It has been shown that the association of this dropout posterior with a log-uniform prior distribution $p(\mathbf{z})$ leads to sparse and interpretable models (Molchanov et al., 2017; Garbarino and Lorenzi, 2021).

Thanks to the flexibility of modern neural network frameworks, it is straightforward to implement non linear parametrizations $\boldsymbol{\mu} = \mathbf{f}^{(\mu)}(\mathbf{x})$ and $\boldsymbol{\Sigma} = \mathbf{f}^{(\sigma)}(\mathbf{x})$ for the mean and covariance functions in the variational and likelihood distributions. Typically it is done by stacking linear or convolution layers, interleaved with non-linear activation functions such as sigmoid and hyperbolic tangent. This modeling is in general highly task-dependent.

3. Experiments

3.1. Illustration on a simplified brain imaging dataset

In this section we describe a simple experiment where we use MT-MCVAE to model the joint relationship between magnetic resonance imaging (MRI) and fluorodeoxyglucose positron emission tomography (FDG-PET) images when there are missing data at training time. The trained model will be then applied on test data to the cross-modality reconstruction problem (MRI to FDG-PET and *vice versa*). Data comes from the 'Adni2' [10] dataset (see details in § 3.3.1, Tab. 3), from which we took the MRI and FDG-PET brain imaging modalities. In what follows, each one of this two modalities corresponds to a specific data view. For each subject ($n = 424$, with both MRI and FDG-PET) we extracted 3 brain slices for each one of the sagittal, coronal, and axial plane. The resulting 3816 slices were randomly allocated to a training and testing set with respectively sizes of 3500 and 316 samples. We downsampled the slices to dimension 28×28 (784 pixels). To simulate a datasets with missing views, we controlled for the fraction of observations with complete views (f) in the training set: this procedure is depicted in Fig. 3 where we show an example of training dataset created with $f = 1/3$. For our experiments we took all the 3500 training images and we randomly removed MRI and FDG-PET views to obtain different training sets for which $f \in \{0, 0.25, 0.5, 0.75, 1\}$. In the case $f = 0$, from each subjects we kept only its MRI or FDG-PET slices, representing the limit case where no direct relationship between views is observable. In the limit case $f = 1$, all MRI and FDG-PET are paired, representing the ideal case of no missing views, that is the working case of the MCVAE (Antelmi et al., 2019). We adopted a deep architecture with 4 layers for both encoders and decoders, having ReLU activation functions and layer dimensions of $784 - 1024 - 1024 - 16$ in the encoding and $16 - 1024 - 1024 - 784$ in the decoding path, an architecture inspired from those used by Andrew et al. (2013) and Wang et al. (2015) for a similar task on the MNIST dataset (LeCun et al., 2010). We adopted a Gaussian likelihood for the decoders, with independent diagonal covariance parameters, and we trained our model with mini-batches of size 500 for 3000 epochs, after setting up the Adam optimizer with a learning rate of 0.001. Training was repeated 5 times, by changing the initialization random seed of the model parameters. In Tab. 2 we show the Mean Squared Error (MSE) and Negative Log-Likelihood

[10] adni.loni.usc.edu. The ADNI was launched in 2003 as a public-private partnership, led by Principal Investigator Michael W. Weiner, MD. For up-to-date information, see www.adni-info.org.

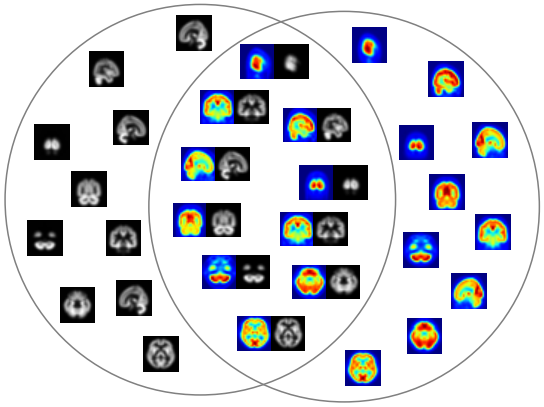

Figure 3: Pictorial example of training an imaging dataset with two views: MRI (left side, in gray scale) and FDG-PET (right side, in color scale). In this case we have data from 30 independent observations: 10 with left-views only; 10 with right-views only; 10 with complete views. The fraction of observations with complete views amounts to: $f = 1/3$.

Table 2: Mean squared error (MSE) and negative log-likelihood (NLL) - the lower the better - measured as mean (st.dev) on the reconstructed brain images of the test-set. The MRI were used to infer the FDG-PET slices in the same subject, and *vice versa*. Results stratified by f, the fraction of observations with no missing views in the training set. Notice the immediate drop in the error metrics as soon as f increases.

f	0.00	0.25	0.50	0.75	1.00
MSE	40.72 (4.31)	1.77 (0.04)	1.63 (0.06)	1.54 (0.03)	1.51 (0.03)
NLL	96.44 (10.33)	0.53 (0.09)	0.16 (0.12)	-0.07 (0.07)	-2.63 (0.03)

(NLL) when predicting MRI from the FDG-PET slices and *vice versa* in the testing set. We notice the immediate drop in the error metrics as soon as the parameter f increases, which means that as the model is fed with an increasing proportion of multi-view data points in the training set, its predictions on the testing set become more precise.

3.2. Synthetic Experiments

In this section we describe our results on extensive synthetic experiments performed with our model and different benchmark methods in two conditions: 1) missing at random views for each dataset, and 2) datasets with systematically missing views (missing not at random).

3.2.1. Data preparation

To simulate multi dataset observations, we sample the latent variable $\mathbf{z}_{d,n}$ from a multivariate Gaussian with zero-mean and identity covariance matrix, and subsequently we transform each sample with random linear mapping towards the observation space to obtain $\mathbf{x}_{d,n,v}$. The detailed procedure is described in *Sup. Mat.* . We then corrupt the observations with increasing levels of noise and we finally remove views in the context of the *missing at random* (MAR) and *missing not at random* (MNAR) experiments.

In the MAR experiments views were randomly removed according to a parameter $0 \leq f \leq 1$, which controls the fraction of data-points with complete views. In the limit case $f = 1$, each data-point has all the views, representing the ideal case of no missing views, that is the working case of the Multi-Channel Variational Autoencoder (Antelmi et al., 2019). In the case $f = 0$, each data-point has one and only one randomly assigned view, representing the extreme case where no direct relationship between views is observable. Here our multi-view model collapses into a disjoint series of independent Variational Autoencoders (Kingma and Welling, 2014; Rezende et al., 2014). In the general case, each data-point has probability f to have all the views, and probability $1 - f$ to have a randomly assigned view out of the total available views. The general case represents the case where the relationship between views can be established only through a fraction f of the total available data-points.

In the MNAR experiments we removed specific views for each simulated dataset, ensuring at the same time the absence of at least one view for a datasets, and the presence of at least one view in common between pairs of datasets. As an example, in the case with three datasets and three views, the association view-dataset can be expressed through the following association matrix A:

$$A = \begin{pmatrix} 1 & 0 & 1 \\ 1 & 1 & 0 \\ 0 & 1 & 1 \end{pmatrix}, \tag{9}$$

where $A(v, d) = 1$ indicates the presence of view v in dataset d. For experimental purposes we limited our MNAR simulations to cases that can be defined with square association matrices having a dimensionality not greater than 5×5.

3.2.2. Model Fitting and Evaluation

In both MAR and MNAR experiments we fit the synthetic scenarios with our model, where we choose a linear Gaussian parametrization for variational and likelihood distributions, made explicit respectively in Eq. (6) and Eq. (7), with a latent dimension matched to the one used to generate the data. We trained our model for 10000 epochs which ensured convergence, after setting up the Adam optimizer with a learning rate of 0.001. For each simulated scenario we predicted the missing views according to Eq. (5) on testing hold-out datasets.

Results, cross-validated on 5 folds, are summarized with the *mean squared error* (MSE) metric on testing hold-out datasets for every simulated scenario. We applied the same evaluation procedure for the benchmark methods.

3.2.3. Benchmark Methods

Among state of the art multivariate linear and non linear imputation methods, we selected the following benchmark approaches: 1) k-Nearest Neighbors (KNN) with $k = \{1, 5\}$; 2) Denoising Autoencoder (DAE) (Gondara and Wang, 2018); 3) Multivariate Imputation by Chained Equations (MICE) (van Buuren and Groothuis-Oudshoorn, 2000).

For the KNN approach we used the *KNNImputer* method as implemented in the *Scikit-Learn* library (Pedregosa et al., 2011). Here each sample's missing values are imputed using the mean value from k nearest neighbors found in the training set, according to their Euclidean distance.

The Denoising Autoencoder, initially developed by Vincent et al. (2008), is based on an overcomplete deep autoencoder. It

maps input data to a higher dimensional space which, in combination with an initial dropout layer inducing corruption, makes the model robust to missing data. We used the same architecture proposed by Gondara and Wang (2018), that is three hidden layers for encoder and decoder networks, Tanh activation functions, hyperparameter $\Theta = 7$, and dropout $p = 0.5$, as they proved to provide consistently better results.

In MICE, as implemented in van Buuren and Groothuis-Oudshoorn (2011), missing values are modeled as a multivariate linear combination of the available features. This methodology is attractive if the multivariate distribution is a reasonable description of the data, which in our case it is by construction. MICE specifies the multivariate imputation model on a variable-by-variable basis by a set of conditional densities, one for each incomplete variable. Starting from an initial imputation, MICE draws imputations by iterating over the conditional densities.

3.2.4. Results

In the synthetic tests our model provides the best performances overall, with a mean MSE improvement compared to the best competing method of 17% in MAR cases and 71% in MNAR cases (Fig. 4). We notice that DAE is not always better than KNN ($k = 5$), especially in low SNR cases. We were able to fit the MICE model only on MNAR cases with high SNR, where it performed poorly (boxplot not shown), while in all the other cases, including all MAR cases, the model did not converge.

In Fig. 5 we show MAR experiments results stratified by SNR and by the fraction f of data-points with complete views. Here we notice how with already $f = 0.25$ we can significantly reduce the prediction error on testing data-points compared to the case $f = 0$, where no relationship between views can be established. Moreover, reaching the ideal case of $f = 1$, that is when there are no missing views in the dataset, does not improve significantly the prediction performance of our model compared to the case $f = 0.25$.

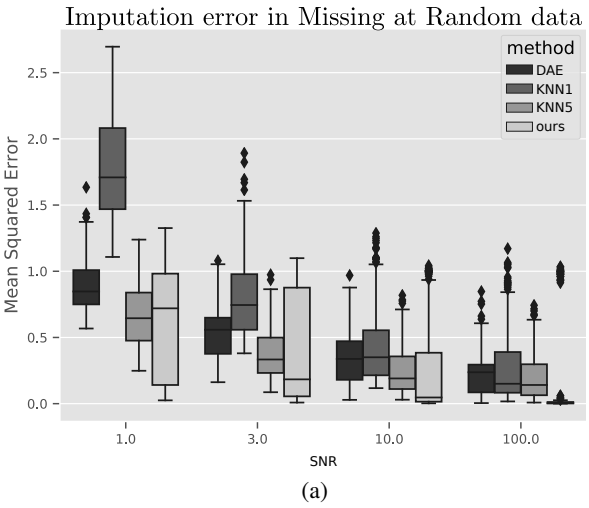

(a)

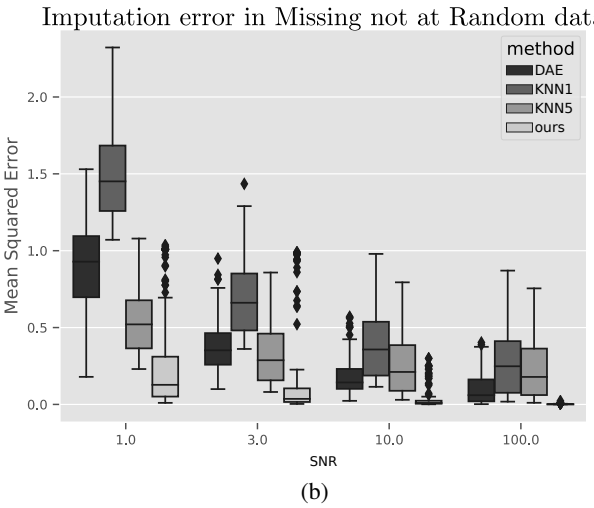

(b)

Figure 4: Mean Squared Error (MSE) of imputation in synthetic held-out datasets (5-folds cross-validation). Compared to the best competing methods among k-Nearest Neighbor ($k = \{1, 5\}$) and Denoise Autoencoder (DAE), our model comes out as the best performer, with a mean MSE improvement of 17% in MAR cases (a) and 71% in MNAR cases (b). Stratification by signal-to-noise ratio (SNR) is shown.

3.3. Experiments on Brain Imaging Data

In this section we describe our results on jointly modeling real medical imaging datasets, independently acquired in the context of dementia studies.

We executed three kinds of experiments: 1) benchmark evaluation of our model against the best competing methods from the previous section; 2) multi-view feature prediction with our model on all the available datasets in multiple training and testing conditions. 3) diagnosis classification from multi-view heterogeneous data in different training and testing conditions.

3.3.1. Data Sources

Data used in the preparation of this section were obtained from the following sources.

1. The Alzheimer's Disease Neuroimaging Initiative (ADNI), a database of brain imaging and related clinical data of cognitively normal subjects, and on patients presenting various degrees of cognitive decline.
2. MIRIAD dataset, a database of brain imaging and related clinical data of cognitively normal subjects and patients affected by Alzheimer's disease (Malone et al., 2013).
3. OASIS-3 dataset, a database of brain imaging and related clinical data of cognitively normal subjects and subjects at various stages of cognitive decline (LaMontagne et al., 2019).
4. A local cohort collected at the Geneva University Hospitals, with brain imaging and related clinical data of patients with various cognitive disorders.

Subjects enrollment, data collection, and data sharing were approved by the ethic committees associated to each study dataset in accordance with the principles of the Declaration of Helsinki.

The available imaging modalities comes from the following acquisitions:

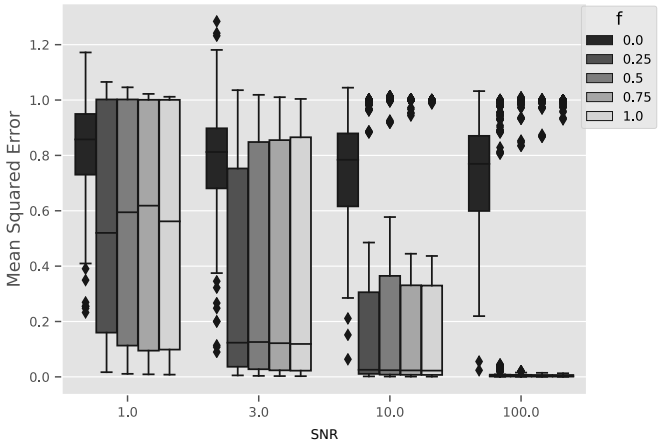

Figure 5: Mean Squared Error of test sets predictions in synthetic held-out datasets in MAR scenarios. Stratification by SNR and by the fraction f of data-points with complete views is shown. A value of $f = 0.25$ is enough to reduce the prediction error on testing data-points at the level of the ideal case ($f = 1$).

1. structural Magnetic Resonance Imaging (MRI) to measure anatomical volumes in the brain;
2. Positron Emission Tomography (PET) with Fluorodeoxyglucose (FDG) tracer, to measure the glucose uptake, which reflects the functional status of the brain;
3. PET with the AV45 tracer, to measure the amyloid deposits in the brain;
4. PET with the AV1451 tracer, to measure the tau protein aggregates in the brain.

We divided the ADNI dataset into two complementary datasets: 'Adni1', composed by subjects recruited in the initial ADNI1 study (2004-2009), and 'Adni2' composed by those subjects subsequently recruited in ADNI-GO, ADNI2, and ADNI3 (2010-ongoing). Data modalities and acquisition protocols of 'Adni1' present differences from those of 'Adni2'. Specifically, in 'Adni1' and 'Adni2' the MRI imaging was performed respectively on 1.5T and 3T scanners. The two cohorts differs also for the presence of PET imaging data. Therefore we consider these two cohorts as separated datasets.

To summarize, we grouped our data into five distinct datasets which we named as follows: 'Adni1', 'Adni2', 'Miriad', 'Oasis3', 'Geneva'.

3.3.2. Imaging Processing

The brain scans were processed in order to have measurements on regions defined in the Desikan-Killiany atlas (Desikan et al., 2006). Brain MRI scans were processed with FreeSurfer [11] (Reuter et al., 2012) to measure brain cortical and sub-cortical volumes, and volumes occupied by the cerebrospinal fluid (CSF), for a total of 99 regions of interest. Relative standardized uptake values (SUVR) were computed for the PET scans (FDG, AV45, AV1451), processed with SPM (Ashburner and Friston, 2000). SUVRs were computed using the cerebellum as reference region, and averaged in the same regions used for the MRI, except those containing the CSF, for a total of 94 regions of interest.

[11] surfer.nmr.mgh.harvard.edu

Table 3: Number of subjects per view available in each dataset. The last columns provide the size of the intersection (∩) and union (∪) of subjects with available views. Notice how in the jont set no subject has all the modalities.

View (# features):	clin (2)	MRI (99)	FDG (94)	AV45 (94)	AV1451 (94)	∩	∪
Dataset							
Adni1	740	730	-	-	-	730	740
Adni2	1324	710	424	417	61	53	1324
Miriad	67	67	-	-	-	67	67
Oasis3	529	489	-	148	-	147	529
Geneva	999	-	65	120	54	15	999
Tot. subjects	3659	1996	489	685	115	0	3659
Tot. datasets	5	4	2	3	2		

3.3.3. Gathering Observations into Views

Observations from the five available datasets (§ 3.3.1) were grouped into the following views.

1. clin: grouping age and the Mini-Mental cognitive score (MMSE).
2. MRI: grouping brain volumes computed with FreeSurfer.
3. FDG: average brain glucose uptake measured through the analysis of FDG-PET scans.
4. AV45: average brain amyloid deposits measured through the analysis of AV45-PET scans.
5. AV1451: average brain tau protein aggregates measured through the analysis of AV1451-PET scans.

For each subject belonging to the 'Adni1', 'Adni2', 'Miriad' and 'Geneva' datasets, we choose the first available time-point, or baseline. In 'oasis3', since measurements were mostly acquired in different days, we choose to pair nearby time points across modalities into a single one. Time interval between views within one subject was minimal (AV45 vs MRI: $\leq$ 90 days, MRI vs clin: $\leq$ 90 days).

In Tab. 3 we show the number of observations stratified by dataset and view. Size of the intersection (∩) and union (∪) of subjects with available views is also provided. Please note that the only view in common across datasets is the clinical one, composed by MMSE and age features only.

We adjusted all the views feature-wise with *ComBat* (Johnson et al., 2007), a normalization method originally develop in genomics, which was adopted in neuroimaging studies to reduce unwanted sources of variation in the data due to the differences in acquisition protocols among datasets (Fortin et al., 2017, 2018; Orlhac et al., 2020). In ComBat, we set the variable 'age' as main regressor, and 'Adni2' as reference dataset for the training set. The ComBat reference dataset for testing was the whole training split.

A final feature-wise standardization step was applied by zero centering the data and by rescaling them to have a unity variance. Standardization parameters were computed on the training sets and applied to training and testing sets.

Table 4: Mean Squared Error (MSE) of test data from Adni2. All models were trained on all the available datasets by holding-out data from the Adni2 test dataset. 5-folds cross validation of MSE is shown as mean (standard deviation). Best results in boldface are significant with an α level of 0.01 with respect to both competing methods.

View	model		
	DAE	KNN5	ours
clin	0.73 (0.14)	0.44 (0.05)	0.45 (0.07)
MRI	1.23 (0.31)	0.88 (0.15)	**0.70** (0.13)
FDG	4.20 (0.56)	4.15 (0.59)	**1.09** (0.15)
AV45	1.45 (0.35)	1.20 (0.25)	**0.89** (0.15)
AV1451	1.54 (0.82)	1.44 (0.83)	**1.05** (0.45)

3.3.4. Experiment 1: Benchmark Validation

The purpose of this experiment is to validate on real data the benchmarked results obtained with the synthetic experiments (§ 3.2).

As benchmark methods, we choose the best performers on the synthetic experiments, namely KNN5 and DAE. We choose for our MT-MCVAE model a linear Gaussian parameterization for the likelihood and sparse variational distributions of Eq. (7) and Eq. (8) respectively, the latter with a latent dimension of 32. We trained it for 20000 epochs which ensured convergence, after setting up the Adam optimizer with a learning rate of 0.001. In testing, we set up a dropout threshold for the latent space of 0.5.

We trained all the models (KNN5, DAE, ours) with data coming from all the datasets except from 'Adni2', left out for testing purposes. We choose the 'Adni2' dataset as testing dataset since it provides all the views, and the highest number of observations per view (Tab. 3).

Prediction performances were evaluated with the Mean Squared Error (MSE) metric, measured on the available views in the testing dataset, reconstructed with Eq. (5). All results were validated by means of 5-folds cross-validation.

Results. In Tab. 4, we show the MSE metric on predicting missing views in the testing dataset with our model and with the benckmark ones. Best results are in boldface, which show a clear advantage of using our model and confirm our findings in the synthetic experiments.

3.3.5. Experiment 2: Feature Prediction

The purpose of this experiment is to compare, in features prediction experiments, the generalization performance the MCVAE model with respect to our new Multi Task extension (MT-MCVE). This experiment was run in three different conditions:

1. Single Task with Internal Benchmark (STIB): when training and testing data are chosen from the same dataset;
2. Single Task with External Benchmark (STEB): when models trained on one dataset are tested on another one;
3. Multi Task Learning (MTL): when models are trained on all the available datasets except the testing one.

In STIB and STEB experiments, both MCVAE and MT-MCVAE models are trained on the same views, but while in MCVAE we need to discard observations with missing views from the training set, with MT-MCVAE we can include them by grouping together observations with common views into homogeneous tasks. In MTL experiments, MCVAE models cannot be trained because no observation has simultaneously all the views.

We choose for both MCVAE and MT-MCVAE a linear Gaussian parameterization for the likelihood and variational distributions as in Eq. (7) and Eq. (8) respectively. Models were trained on all the available views in the training dataset. We trained them for 20000 epochs which ensured convergence, after setting up the Adam optimizer with a learning rate of 0.001. Prediction performances were evaluated with the Mean Squared Error (MSE) metric, measured on the available views in the testing dataset, reconstructed with Eq. (5).

Non-linear experiments were also made on the MTL scenarios with our MT-MCVAE model, where the encoding and decoding distributions were parametrized with neural networks with up to 4 layers and LeakyReLU activation functions. In this case we choose hidden dimension as the mean value between the input features and latent dimension (32 features), rounded towards the nearest integer (*e.g.,* for the MRI views and a depth of 3 layers we used a symmetric encoding-decoding architecture with dimensions: 99 – 66 – 66 – 32 – 66 – 66 – 99). Training for 20000 epochs with Adam and a learning rate of 0.001 ensured convergence.

All results were validated by means of 5-folds cross-validation.

Results. In Tab. 5 and Tab. 6 we show the prediction error in terms of MSE for each test dataset and view, on the three experimental conditions described earlier.

In STIB and STEB cases (Tab. 5), the MT-MCVAE model performs either similarly or statistically better than the MCVAE, especially in cases where the difference between the union and intersection set of observations is higher (cfr. Tab. 3).

In the MTL scenario (Tab. 6) there are 12 cases that could be fitted with MT-MCVAE only. We measure an overall better performance of MTL with respect to STIB (7/12 of cases) and with respect to STEB (10/12 of cases).

In Tab. 7, the results on a non linear application of our method in MTL cases show that no improvement is gained when changing the architecture depth (anova test, alpha level 0.05).

3.3.6. Experiment 3: Diagnosis Prediction

The purpose of this experiment is to compare, in diagnosis prediction experiments, the generalization performance of the MCVAE model with respect to the MT-MCVAE, in the three experimental conditions described earlier: STIB, STEB, and MTL. Diagnostic classes are: Alzheimer's disease (AD), mild cognitive impairment (MCI), normal cognition (NC).

For both MCVAE and MT-MCVAE we choose a linear Gaussian parameterization for the variational distributions as in Eq. (8). To adapt the models to this new classification experiment, we adopt as decoding function for the latent variable $\mathbf{z}$,

Table 5: Mean Squared Reconstruction Error (the lower the better) measured on test dataset views (clinical scores and imaging derived phenotypes) predicted with the Multi-Channel VAE (MCVAE) and the Multi Task MCVAE (MT-MCVAE). 5-folds cross-validation results shown as average (standard deviation). Models were trained on all the available views in the training dataset, independently of their presence in the testing dataset. Experiments were run in two different conditions: 1) when training and testing data are chosen from the same dataset, or Single Task with Internal Benchmark (STIB) learning case; 2) when models trained on one dataset are tested on another dataset, or Single Task with External Benchmark (STEB) case; In all cases the MT-MCVAE performs either similarly or statistically better than the MCVAE, with alpha levels at 0.05 (*), 0.01 (**), and 0.001 (***).

		view	clin		MRI		FDG		AV45		AV1451	
		model	MCVAE	MT-MCVAE	MCVAE	MT-MCVAE	MCVAE	MT-MCVAE	MCVAE	MT-MCVAE	MCVAE	MT-MCVAE
test dataset	condition	train dataset										
Adni1	STIB	Adni1	0.90 (0.12)	0.89 (0.13)	0.85 (0.11)	0.83 (0.12)*	-	-	-	-	-	-
	STEB	Adni2	0.91 (0.17)	0.77 (0.13)*	1.02 (0.23)	0.85 (0.11)***	-	-	-	-	-	-
		Miriad	0.96 (0.17)	1.14 (0.27)	0.80 (0.14)	0.82 (0.13)*	-	-	-	-	-	-
		Geneva	-	-	-	-	-	-	-	-	-	-
		Oasis3	0.83 (0.30)	0.54 (0.10)*	0.80 (0.15)	0.76 (0.11)*	-	-	-	-	-	-
Adni2	STIB	Adni2	0.83 (0.11)	0.73 (0.15)	0.74 (0.13)	0.70 (0.11)**	0.73 (0.14)	0.59 (0.10)***	1.03 (0.19)	0.80 (0.10)***	1.33 (0.59)	1.18 (0.52)*
	STEB	Adni1	0.77 (0.18)	0.80 (0.14)	0.74 (0.11)	0.75 (0.12)	-	-	-	-	-	-
		Miriad	0.73 (0.20)	0.71 (0.18)	0.78 (0.13)	0.77 (0.13)	-	-	-	-	-	-
		Geneva	0.47 (0.06)	0.48 (0.09)	-	-	1.40 (0.21)	1.09 (0.15)***	1.10 (0.21)	0.91 (0.15)**	1.34 (0.52)	1.05 (0.45)***
		Oasis3	0.76 (0.23)	0.61 (0.13)	0.68 (0.12)	0.68 (0.11)	-	-	1.32 (0.29)	1.13 (0.26)***	-	-
Gneva	STIB	Geneva	0.79 (0.34)	0.98 (0.52)	-	-	3.63 (1.35)	3.18 (1.04)*	1.82 (0.57)	1.76 (0.47)*	1.27 (0.82)	1.19 (0.67)*
	STEB	Adni1	-	-	-	-	-	-	-	-	-	-
		Adni2	2.57 (1.09)	2.07 (1.05)	-	-	3.01 (1.05)	2.69 (0.77)*	1.92 (0.90)	1.41 (0.39)	1.81 (0.81)	1.42 (0.66)***
		Miriad	-	-	-	-	-	-	-	-	-	-
		Oasis3	1.93 (0.66)	2.28 (0.89)	-	-	-	-	1.70 (0.51)	1.63 (0.55)*	-	-
Miriad	STIB	Miriad	3.21 (1.07)	3.23 (2.55)	6.39 (1.57)	6.38 (1.52)	-	-	-	-	-	-
	STEB	Adni1	6.90 (3.33)	6.49 (3.42)	6.60 (1.61)	6.73 (1.55)	-	-	-	-	-	-
		Adni2	5.60 (2.76)	3.97 (3.14)	5.93 (1.90)	6.59 (1.64)	-	-	-	-	-	-
		Geneva	-	-	-	-	-	-	-	-	-	-
		Oasis3	6.80 (6.52)	6.24 (4.62)	6.29 (1.68)	6.23 (1.40)	-	-	-	-	-	-
Oasis3	STIB	Oasis3	0.83 (0.33)	0.68 (0.28)	0.68 (0.13)	0.66 (0.12)*	-	-	1.58 (0.63)	1.22 (0.26)***	-	-
	STEB	Adni1	1.20 (0.25)	1.23 (0.28)	0.78 (0.14)	0.79 (0.14)	-	-	-	-	-	-
		Adni2	1.11 (0.33)	1.09 (0.24)	0.89 (0.18)	0.76 (0.15)***	-	-	0.94 (0.22)	1.02 (0.26)*	-	-
		Miriad	0.98 (0.21)	1.02 (0.20)	0.83 (0.18)	0.83 (0.18)	-	-	-	-	-	-
		Geneva	0.55 (0.28)	0.49 (0.26)	-	-	-	-	1.23 (0.61)	1.11 (0.26)*	-	-

Table 6: Mean Squared Reconstruction Error (the lower the better) measured on test dataset views (clinical scores and imaging derived phenotypes) predicted with our model. 5-folds cross-validation results shown as as average (standard deviation). Models were trained on all the available views in the training dataset, independently of their presence in the testing dataset. Experiments were run in three different conditions: 1) when training and testing data are chosen from the same dataset, or Single Task with Internal Benchmark (STIB) learning case; 2) when models trained on one dataset are tested on another dataset, or Single Task with External Benchmark (STEB) case; 3) when models are trained on all the available datasets except the testing one, or Multi Task Learning (MTL). We measure a better performance in the MTL condition with respect to the STIB (§) in $7/12$ of cases, and in $10/12$ of cases with respect to the average STEB (†) experiments.

	view	clin	MRI	AV45
test dataset	condition			
Adni1	STIB	0.89 (0.13)	0.83 (0.12)	-
	STEB (avg)	0.82 (0.17)	0.81 (0.12)	-
	MTL	0.45 (0.07)§†	0.77 (0.10)§†	-
Adni2	STIB	0.73 (0.15)	0.70 (0.11)	0.80 (0.10)
	STEB (avg)	0.65 (0.14)	0.73 (0.12)	1.02 (0.21)
	MTL	0.45 (0.07)§†	0.70 (0.13)†	0.89 (0.15)†
Geneva	STIB	0.98 (0.52)	-	1.76 (0.47)
	STEB (avg)	2.18 (0.97)	-	1.52 (0.47)
	MTL	1.80 (1.16)†	-	1.35 (0.37)§†
Miriad	STIB	3.23 (2.55)	6.38 (1.52)	-
	STEB (avg)	5.57 (3.73)	6.52 (1.53)	-
	MTL	2.31 (1.65)§†	6.17 (1.37)§†	-
Oasis3	STIB	0.68 (0.28)	0.66 (0.12)	1.22 (0.26)
	STEB (avg)	0.96 (0.25)	0.79 (0.16)	1.07 (0.26)
	MTL	0.72 (0.09)†	0.81 (0.15)	1.09 (0.30)§

Table 7: Mean Squared Reconstruction Error (mean (st.dev.), the lower the better) measured on clinical scores and imaging derived phenotypes predicted with our MT-MCVAE model in MTL experiments. Results stratified by the number of layers in the encoder-decoder architecture. We measure no significant differences among architectures (anova statistical test at an alpha level of 0.05). Best overall results in boldface.

#layers	1	2	3	4
clin	**0.97** (0.49)	1.05 (0.65)	1.04 (0.60)	1.02 (0.50)
MRI	**2.09** (0.92)	2.14 (0.69)	2.13 (0.68)	2.13 (0.68)
AV45	**1.09** (0.29)	1.16 (0.25)	1.15 (0.26)	1.15 (0.25)

Table 8: Number of subjects stratified by dataset and diagnosis: Alzheimer's Disease (AD); Mild Cognitive Impairment (MCI); Normal Cognition (NC).

	AD	MCI	NC	other	total
Adni1	403	172	165	-	740
Adni2	328	455	541	-	1324
Geneva	147	405	-	447	999
Miriad	44	-	23	-	67
Oasis3	149	-	380	-	529

Table 9: Experiment of diagnosis classification run with the Multi-Channel VAE (MCVAE) and the Multi Task MCVAE (MT-MCVAE). 5-folds classification accuracy in % is shown as mean (standard deviation). Since there are no MCI in miriad and oasis3 datasets, the classification tests 'AD vs MCI' and 'MCI vs NC' are meaningless and not reported. Since there are no NC in the geneva dataset, the classification tests 'AD vs NC' and 'MCI vs NC' are meaningless and not reported. Experiments were run in two different conditions: 1) when training and testing data are chosen from the same dataset, or Single Task with Internal Benchmark (STIB) learning case; 2) when models trained on one dataset are tested on another dataset, or Single Task with External Benchmark (STEB) case. In all cases the MT-MCVAE model performs either similarly or statistically better than the MCVAE, with alpha levels at 0.05 (*), 0.01 (**), and 0.001 (***).

		classification task	AD vs MCI		AD vs NC		MCI vs NC	
		model	MCVAE	MT-MCVAE	MCVAE	MT-MCVAE	MCVAE	MT-MCVAE
test dataset	condition	train dataset						
Adni1	STIB	Adni1	72.70 (3.72)	72.87 (4.37)	81.69 (2.97)	81.51 (3.14)	62.00 (8.91)	62.90 (8.72)
	STEB	Adni2	47.48 (3.56)	58.96 (3.55)***	68.50 (4.86)	73.77 (2.80)*	53.12 (6.42)	59.65 (2.76)*
		Miriad	-	-	82.58 (4.75)	80.82 (3.16)	-	-
		Oasis3	-	-	48.57 (6.48)	62.31 (6.43)**	-	-
		Geneva	36.52 (5.29)	46.61 (8.03)*	-	-	-	-
Adni2	STIB	Adni2	50.58 (3.90)	80.07 (2.53)***	82.86 (3.28)	87.92 (3.46)*	58.63 (4.27)	65.56 (1.11)**
	STEB	Adni1	57.59 (2.61)	58.23 (2.87)	64.21 (3.36)	64.21 (3.52)	63.05 (2.00)	62.75 (1.80)
		Miriad	-	-	70.32 (7.29)	70.20 (7.17)	-	-
		Oasis3	-	-	68.24 (2.97)	75.72 (1.90)**	-	-
		Geneva	64.49 (2.98)	63.98 (3.30)	-	-	-	-
Geneva	STIB	Geneva	65.76 (3.62)	77.70 (8.12)*	-	-	-	-
	STEB	Adni1	29.17 (5.87)	30.08 (5.49)	-	-	-	-
		Adni2	38.61 (15.08)	70.11 (2.90)**	-	-	-	-
Miriad	STIB	Miriad	-	-	83.85 (13.84)	86.70 (15.68)	-	-
	STEB	Adni1	-	-	74.18 (14.37)	74.18 (14.37)	-	-
		Adni2	-	-	74.95 (11.58)	78.90 (11.54)*	-	-
		Oasis3	-	-	45.71 (18.08)	66.04 (19.35)	-	-
Oasis3	STIB	Oasis3	-	-	74.47 (2.49)	80.35 (3.59)*	-	-
	STEB	Adni1	-	-	49.16 (6.34)	48.22 (5.78)	-	-
		Adni2	-	-	67.86 (3.80)	75.42 (4.68)*	-	-
		Miriad	-	-	64.48 (8.65)	62.02 (9.74)	-	-

Table 10: Experiment of diagnosis classification run with our model. 5-folds classification accuracy in % is shown as mean (standard deviation). Experiments were run in three different conditions: 1) when training and testing data are chosen from the same dataset, or Single Task with Internal Benchmark (STIB) learning case; 2) when models trained on one dataset are tested on another dataset, or Single Task with External Benchmark (STEB) case; 3) when models are trained on all the available datasets except the testing one, or Multi Task Learning (MTL). In all cases we measure a better performance in the MTL condition with respect to the average STEB one (†).

	classification task	AD vs MCI	AD vs NC
test dataset	condition		
Adni1	STIB	72.87 (4.37)	81.51 (3.14)
	STEB (avg)	52.79 (5.79)	72.30 (4.13)
	MTL	59.30 (2.08)†	81.86 (3.26)†
Adni2	STIB	80.07 (2.53)	87.92 (3.46)
	STEB (avg)	61.11 (3.09)	70.04 (4.20)
	MTL	67.82 (1.91)†	85.16 (2.13)†
Geneva	STIB	77.70 (8.12)	-
	STEB (avg)	50.10 (4.20)	-
	MTL	52.54 (4.82)†	-
Miriad	STIB	-	86.70 (15.68)
	STEB (avg)	-	73.04 (15.09)
	MTL	-	98.46 (3.44)†
Oasis3	STIB	-	80.35 (3.59)
	STEB (avg)	-	61.89 (6.73)
	MTL	-	77.70 (4.22)†

the following Categorical likelihood:

$$p\left(y_{d,n}|\mathbf{z},\boldsymbol{\theta}\right) = \mathrm{Cat}\left(\pi = \boldsymbol{\theta}\mathbf{z}\right), \tag{10}$$

where $y_{d,n}$ is the diagnosis associated to the data-point n in the dataset d. The probability vector π is a two dimensional vector representing the class probability for each of the three binary comparisons across the three diagnostic classes, namely AD *vs* MCI, AD *vs* NC, MCI *vs* NC ,and is parametrized with a linear transformation of the latent $\mathbf{z}$ by the matrix $\boldsymbol{\theta}$.

Non-linear experiments were also made on the MTL scenarios with our MT-MCVAE model, benchmarked against the EmbraceNet method (Choi and Lee, 2019), where the encoding distributions were parametrized with neural networks with up to 4 layers and LeakyReLU activation functions. Training for 20000 epochs with the Adam optimizer and a learning rate of 0.001 ensured convergence.

Models were trained on all the available views in the training dataset, independently of their presence in the testing dataset. Classes probabilities were inferred from the all the available views in the testing dataset with the following equation:

$$\hat{y}_{d,n} = \frac{1}{V_{d,n}} \sum_{w=1}^{V_{d,n}} \mathbb{E}_{q_{d,n,w}(\mathbf{z})}\left[p\left(y_{d,n}|\mathbf{z},\boldsymbol{\theta}\right)\right]. \tag{11}$$

We attributed to each subject the diagnostic class with the highest inferred probability.

The performance on test datasets was evaluated by measuring the classification accuracy (%). All results were validated by means of 5-folds cross-validation.

Results. In Tab. 9 we show the classification accuracy of MCVAE and MT-MCVAE. In STIB and STEB cases, the MT-MCVAE model performs either similarly or statistically better than the MCVAE. There are 7 cases in the MTL condition (Tab. 10) that could be fitted with the MT-MCVAE model only. In all of them we measure a better performance with respect to the best STEB cases.

In Tab. 11, the results on a non linear application of our method in MTL cases show that no improvement is gained when changing the architecture depth (anova test, alpha level 0.05) for both the EmbraceNet and MT-MCVAE models. No significant differences (t-test, alpha level 0.05) are detectable between the EmbraceNet and MT-MCVAE models for any given architecture depth level. This result show that on the classification task the MT-MCVAE is equivalent to advanced MTL approaches from the state of the art.

4. Discussion

In both the experiments on synthetic and real data, our model compared favorably with respect to state of the art benchmark methods.

An interesting result is the one presented in Fig. 5, suggesting that collecting a minimum amount of data-points with complete views is enough for our model to capture the joint relationship among views. The empirical bound on this minimum level of data-points with all available views amounts to 25%. In fact, in our synthetic tests, training on scenarios with completeness level above this bound does not seem to improve significantly the testing results. This condition may be explained by the high collinearity between features due to the linear mappings used to generate the multi-view data. The same bound may be noticed also in our showcase experiment (§ 3.1) where we jointly modeled MRI and FDG-PET brain images. This results suggest that our model can reach its highest prediction power also when data collection resources are scarce, such as in studies were the acquisition of complete observations is hampered by economical reasons or subject dropout.

As a secondary result, we report the positive performance of knn (k = 5) in synthetic scenarios, especially in low snr cases, and on real data experiment, were it is most of the time superior to the DAE. This finding is corroborated by Platias and Petasis (2020) were knn is found to be superior to methods based on autoencoders.

The experimental results on real medical imaging datasets (Tab. 5, Tab. 9) show on the horizontal axes the clear improvement of our MT-MCVAE method with respect to the MCVAE, that inspired our work, given the very same training and testing conditions for both of models. The features and diagnosis prediction clearly improves when using our method, that allows to not discard observations with missing views in the training phase. On the same tables, when read on the vertical axes, we note that models trained and tested on the same single dataset (STIB cases) tend to be more accurate than those trained on multiple other datasets (STEB cases). This is an expected result pointing to the issue of "domain shift", i.e. when observations coming from different datasets are not identically distributed,

Table 11: Diagnosis classification with our model and the EmbraceNet (EN, Choi and Lee (2019)). Accuracy in % as mean (st.dev.) over 5-folds. Results are stratified by the classification task and by the number of layers in the encoder-decoder architecture. We measure no significant difference among architectures depth (anova test, alpha level 0.05) and between models (t-test, alpha level 0.05).

	#layers:	1		2		3		4	
	model:	ours	EN	ours	EN	ours	EN	ours	EN
classification task	condition								
AD vs NC	MTL (avg)	85.79 (3.26)	85.34 (2.30)	79.04 (5.56)	77.68 (4.86)	79.78 (5.92)	78.60 (5.34)	82.47 (4.11)	77.12 (7.22)
AD vs MCI	MTL (avg)	59.89 (2.94)	61.02 (3.47)	56.93 (5.02)	61.38 (3.21)	56.55 (5.33)	62.07 (3.59)	57.49 (6.03)	61.29 (5.04)

leading to generally high "within task" accuracy, and low generalization ability in the "between task" setting. We want to emphasize that we mitigated this problem with a data harmonization step based on ComBat (Johnson et al., 2007), one of the state-of-the-art normalization method in biomedical applications (Fortin et al., 2017, 2018; Orlhac et al., 2020). For this reason, we believe that the domain shift has a marginal impact for the application proposed in our study, and that those differences on the vertical axes are most likely due to the large variety of number of observations, available views, and differences in stratification by diseases in the datasets (*cf.* Tab. 3, Tab. 8).

In feature prediction experiments (Tab. 6) we showed that MT-MCVAE models trained jointly on multiple neuroimaging datasets (ADNI, MIRIAD, OASIS-3, Geneva cohort) perform generally better than the ones trained on a single dataset. We suspect that there are two reasons explaining these results. The first is that modeling simultaneously multiple datasets with our method brings more variability and information at play, making the generalization to unseen data less prone to prediction errors. The second reason maybe that every decoder, associated to its specific view, acts, through the shared latent space, as a regularizer for all the other decoders.

In experiments where we seek to classify subjects to predict their cognitive status (Tab. 10), the MT-MCVAE generalizes better to new unseen datasets when trained jointly on multiple datasets (MTL cases) with respect to cases where the training happens on a single dataset. We notice that the best results happen in cases where testing data and training data come from the same dataset (ST cases), that is when the testing dataset is not anymore unseen to our model. This is a different result than the analogous one in the feature prediction experiments, and we argue that the reason may be due to the lack of the regularization mechanism induced by having concurring decoders. Indeed, the MT-MCVAE classifier is composed by a single decoder only, which can become highly specialized in decoding testing data coming from the same dataset of the training data.

In our non linear experiments we did not capture any improvement by using deep architectures with respect to simple linear mappings, in both feature prediction (Tab. 7) and classification tasks (Tab. 11) on real neuroimaging datasets. These results are in line with our previous work (Antelmi et al., 2019), were we benchmarked other auto-encoding based methods on observations coming from the ADNI dataset. We suspect that this result is due to the general high heterogeneity and relatively small sample size of typical neuroimaging data. Our results on the classification task in multi-view and multi-dataset problem also showed that our approach is equivalent to the EmbraceNet (Choi and Lee, 2019) recently proposed in the literature (§ 3.3.6). While this finding indicates the ability of MT-MCVAE to provide results compatible with the state of the art in MTL classification problems, we note that the architecture of our framework enables a much larger set of applications than the one tackled by the EmbraceNet, such as cross-modality reconstruction and cross-dataset dimensionality reduction.

In our work we have thoroughly investigated architectures with a one-to-one correspondence between encoding and decoding views. This makes our model part of the family of the auto-encoders, where the model acts as identity transformation between the input and the output. Other architectures are nevertheless possible, such as the classifier described in § 3.3.6 In general, there may be an m-to-n relationship, with partially overlapping views among m input views and n output views. Investigating the properties of all the possible architectures is beyond the scope of this work.

As final remark, we want to stress that our model is based on the assumption of independent and identical distributed observations. This assumption may be limiting in healthcare datasets, such as the ones used in this work. In our work we mitigated these biases by harmonizing the datasets before applying our model, and we leave the extension and development of a bias-transparent multi-view models to future works.

5. Conclusions

We proposed a new multi-task latent variable generative model able to learn simultaneously from multiple datasets, even in the presence of non-overlapping views among all the datasets. The available overlap between pairs of datasets allows the information to flow through all the views in the dataset pool. Since the learned view-specific parameters are shared among datasets, missing views can be automatically imputed for every dataset. The method proposed in this work is a coherent extension of classical variational generative models, making the training fast and scalable. Being dataset agnostic, our method allows to integrate all the available data into a joint model, gathering all the available information from multiple datasets at the same time. We conducted extensive tests for the joint modeling of synthetically generated data and of multi-modal neuroimaging datasets from independent dementia studies and associated clinical data, showing the competitiveness of our method with respect to the state of the art. Thanks to its general formulation, the proposed method can find applications beyond the neuroimaging research field.

Declaration of interests

The authors declare that they have no known competing financial interests or personal relationships that could have appeared to influence the work reported in this paper.

Acknowledgments

This work has been supported by:

- the French government, through the UCA^{JEDI} Investments in the Future project managed by the National Research Agency (ANR) with the reference number ANR-15-IDEX-01;

- the French government, through the 3IA Côte d'Azur Investments in the Future project managed by the National Research Agency (ANR) with the reference number ANR-19-P3IA-0002;

- the OPAL infrastructure from Université Côte d'Azur, providing computational resources and support;

- the "Centre de la Mémoire" at Geneva University Hospitals, funded by private donors: A.P.R.A. - Association Suisse pour la Recherche sur la Maladie d'Alzheimer, Genève; Fondation Segré, Genève; Ivan Pictet, Genève; Fondazione Agusta, Lugano; Fondation Chmielewski, Genève. Competitive research projects have been funded by: H2020, Human Brain Project, Innovative Medicines Initiative (IMI), IMI2, Swiss National Science Foundation (project numbers: 169876, 185028, 182772); VELUX Foundation (project number 1123).

- Data collection and sharing for this project was funded by the Alzheimer's Disease Neuroimaging Initiative (ADNI) (National Institutes of Health Grant U01 AG024904) and DOD ADNI (Department of Defense award number W81XWH-12-2-0012). ADNI is funded by the National Institute on Aging, the National Institute of Biomedical Imaging and Bioengineering, and through generous contributions from the following: AbbVie, Alzheimer's Association; Alzheimer's Drug Discovery Foundation; Araclon Biotech; BioClinica, Inc.; Biogen; Bristol-Myers Squibb Company; CereSpir, Inc.; Cogstate; Eisai Inc.; Elan Pharmaceuticals, Inc.; Eli Lilly and Company; EuroImmun; F. Hoffmann-La Roche Ltd and its affiliated company Genentech, Inc.; Fujirebio; GE Healthcare; IXICO Ltd.; Janssen Alzheimer Immunotherapy Research & Development, LLC.; Johnson & Johnson Pharmaceutical Research & Development LLC.; Lumosity; Lundbeck; Merck & Co., Inc.; Meso Scale Diagnostics, LLC.; NeuroRx Research; Neurotrack Technologies; Novartis Pharmaceuticals Corporation; Pfizer Inc.; Piramal Imaging; Servier; Takeda Pharmaceutical Company; and Transition Therapeutics. The Canadian Institutes of Health Research is providing funds to support ADNI clinical sites in Canada. Private sector contributions are facilitated by the Foundation for the National Institutes of Health (`www.fnih.org`). The grantee organization is the Northern California Institute for Research and Education, and the study is coordinated by the Alzheimer's Therapeutic Research Institute at the University of Southern California. ADNI data are disseminated by the Laboratory for NeuroImaging at the University of Southern California.

- Data used in the preparation of this article were obtained also from the MIRIAD database. The MIRIAD investigators did not participate in analysis or writing of this report. The MIRIAD dataset is made available through the support of the UK Alzheimer's Society (Grant RF116). The original data collection was funded through an unrestricted educational grant from GlaxoSmithKline (Grant 6GKC).

- Data were also provided by OASIS-3: Principal Investigators: T. Benzinger, D. Marcus, J. Morris; NIH P50AG00561, P30NS09857781, P01AG026276, P01AG003991, R01AG043434, UL1TR000448, R01EB009352. AV-45 doses were provided by Avid Radiopharmaceuticals, a wholly owned subsidiary of Eli Lilly. Avid has no involvement in study design or analysis.

References

Abi Nader, C., Ayache, N., Robert, P., Lorenzi, M., 2020. Monotonic Gaussian Process for spatio-temporal disease progression modeling in brain imaging data. Neuroimage 205, 116266.

Andrew, G., Arora, R., Bilmes, J., Livescu, K., 2013. Deep Canonical Correlation Analysis. Proc. Mach. Learn. Res. 28, 1247–1255.

Antelmi, L., Ayache, N., Robert, P., Lorenzi, M., 2019. Sparse Multi-Channel Variational Autoencoder for the Joint Analysis of Heterogeneous Data, in: Chaudhuri, K., Salakhutdinov, R. (Eds.), Proc. 36th Int. Conf. Mach. Learn., PMLR. pp. 302–311.

Ashburner, J., Friston, K.J., 2000. Voxel-based morphometry–the methods. Neuroimage 11, 805–21.

Blei, D.M., Kucukelbir, A., McAuliffe, J.D., 2017. Variational Inference: A Review for Statisticians. J. Am. Stat. Assoc. 112, 859–877. doi:10.1080/01621459.2017.1285773.

Buch, A.M., Liston, C., 2020. Dissecting diagnostic heterogeneity in depression by integrating neuroimaging and genetics. Neuropsychopharmacology doi:10.1038/s41386-020-00789-3.

van Buuren, S., Groothuis-Oudshoorn, C.G.M., 2000. Multivariate Imputation by Chained Equations: MICE V1.0 User manual. volume PG/VGZ/00.038. TNO Prevention and Health, Leiden.

Caruana, R., 1998. Multitask Learning. Springer US, Boston, MA. pp. 95–133. doi:10.1007/978-1-4615-5529-2_5.

Chartsias, A., Papanastasiou, G., Wang, C., Semple, S., Newby, D.E., Dharmakumar, R., Tsaftaris, S.A., 2021. Disentangle, Align and Fuse for Multimodal and Semi-Supervised Image Segmentation. IEEE Trans. Med. Imaging 40, 781–792.

Chen, T., Ma, X., Liu, X., Wang, W., Feng, R., Chen, J., Yuan, C., Lu, W., Chen, D.Z., Wu, J., 2019. Multi-view Learning with Feature Level Fusion for Cervical Dysplasia Diagnosis, pp. 329–338. doi:10.1007/978-3-030-32239-7_37.

Choi, J.H., Lee, J.S., 2019. EmbraceNet: A robust deep learning architecture for multimodal classification. Inf. Fusion 51, 259–270.

Desikan, R.S., Ségonne, F., Fischl, B., Quinn, B.T., Dickerson, B.C., Blacker, D., Buckner, R.L., Dale, A.M., Maguire, R.P., Hyman, B.T., Albert, M.S., Killiany, R.J., 2006. An automated labeling system for subdividing the human cerebral cortex on MRI scans into gyral based regions of interest. Neuroimage doi:10.1016/j.neuroimage.2006.01.021.

Dorado-Moreno, M., Navarin, N., Gutiérrez, P., Prieto, L., Sperduti, A., Salcedo-Sanz, S., Hervás-Martínez, C., 2020. Multi-task learning for the prediction of wind power ramp events with deep neural networks. Neural Networks 123, 401–411. doi:10.1016/j.neunet.2019.12.017.

Finn, C., Abbeel, P., Levine, S., 2017. Model-Agnostic Meta-Learning for Fast Adaptation of Deep Networks. PMLR 70, 1126–1135.

Fortin, J.P., Cullen, N., Sheline, Y.I., Taylor, W.D., Aselcioglu, I., Cook, P.A., Adams, P., Cooper, C., Fava, M., McGrath, P.J., McInnis, M., Phillips, M.L., Trivedi, M.H., Weissman, M.M., Shinohara, R.T., 2018. Harmonization of cortical thickness measurements across scanners and sites. Neuroimage 167, 104–120.

Fortin, J.P., Parker, D., Tunç, B., Watanabe, T., Elliott, M.A., Ruparel, K., Roalf, D.R., Satterthwaite, T.D., Gur, R.C., Gur, R.E., Schultz, R.T., Verma, R., Shinohara, R.T., 2017. Harmonization of multi-site diffusion tensor imaging data. Neuroimage 161, 149–170. doi:10.1016/j.neuroimage.2017.08.047.

Garbarino, S., Lorenzi, M., 2021. Investigating hypotheses of neurodegeneration by learning dynamical systems of protein propagation in the brain. Neuroimage , 117980.

Golriz Khatami, S., Robinson, C., Birkenbihl, C., Domingo-Fernández, D., Hoyt, C.T., Hofmann-Apitius, M., 2020. Challenges of Integrative Disease Modeling in Alzheimer's Disease. Front. Mol. Biosci. 6. doi:10.3389/fmolb.2019.00158.

Gondara, L., Wang, K., 2018. Mida: Multiple imputation using denoising autoencoders, in: Phung, D., Tseng, V.S., Webb, G.I., Ho, B., Ganji, M., Rashidi, L. (Eds.), Advances in Knowledge Discovery and Data Mining, Springer International Publishing, Cham. pp. 260–272.

Johnson, W.E., Li, C., Rabinovic, A., 2007. Adjusting batch effects in microarray expression data using empirical Bayes methods. Biostatistics 8, 118–127. doi:10.1093/biostatistics/kxj037.

Kingma, D.P., Salimans, T., Welling, M., 2015. Variational Dropout and the Local Reparameterization Trick, in: Cortes, C., Lawrence, N.D., Lee, D.D., Sugiyama, M., Garnett, R. (Eds.), Adv. Neural Inf. Process. Syst. 28. Curran Associates, Inc., pp. 2575–2583.

Kingma, D.P., Welling, M., 2014. Auto-Encoding Variational Bayes, in: Proc. 2nd Int. Conf. Learn. Represent. (ICLR2014).

LaMontagne, P.J., Benzinger, T.L., Morris, J.C., Keefe, S., Hornbeck, R., Xiong, C., Grant, E., Hassenstab, J., Moulder, K., Vlassenko, A., Raichle, M.E., Cruchaga, C., Marcus, D., 2019. Oasis-3: Longitudinal neuroimaging, clinical, and cognitive dataset for normal aging and alzheimer disease. medRxiv doi:10.1101/2019.12.13.19014902.

Le Sueur, H., Bruce, I.N., Geifman, N., 2020. The challenges in data integration – heterogeneity and complexity in clinical trials and patient registries of Systemic Lupus Erythematosus. BMC Med. Res. Methodol. 20, 164. doi:10.1186/s12874-020-01057-0.

LeCun, Y., Cortes, C., Burges, C., 2010. Mnist handwritten digit database. ATT Labs [Online]. Available: http://yann.lecun.com/exdb/mnist 2.

Liu, J., Calhoun, V.D., 2014. A review of multivariate analyses in imaging genetics. Front. Neuroinform. 8, 29.

Malone, I.B., Cash, D., Ridgway, G.R., MacManus, D.G., Ourselin, S., Fox, N.C., Schott, J.M., 2013. MIRIAD—Public release of a multiple time point Alzheimer's MR imaging dataset. Neuroimage 70, 33–36. doi:10.1016/j.neuroimage.2012.12.044.

Molchanov, D., Ashukha, A., Vetrov, D., 2017. Variational Dropout Sparsifies Deep Neural Networks. arXiv .

Orlhac, F., Lecler, A., Savatovski, J., Goya-Outi, J., Nioche, C., Charbonneau, F., Ayache, N., Frouin, F., Duron, L., Buvat, I., 2020. How can we combat multicenter variability in MR radiomics? Validation of a correction procedure. Eur. Radiol. doi:10.1007/s00330-020-07284-9.

Paszke, A., Gross, S., Massa, F., Lerer, A., Bradbury, J., Chanan, G., Killeen, T., Lin, Z., Gimelshein, N., Antiga, L., Desmaison, A., Kopf, A., Yang, E., DeVito, Z., Raison, M., Tejani, A., Chilamkurthy, S., Steiner, B., Fang, L., Bai, J., Chintala, S., 2019. Pytorch: An imperative style, high-performance deep learning library, in: Wallach, H., Larochelle, H., Beygelzimer, A., d'Alché Buc, F., Fox, E., Garnett, R. (Eds.), Advances in Neural Information Processing Systems 32. Curran Associates, Inc., pp. 8024–8035.

Pedregosa, F., Varoquaux, G., Gramfort, A., Michel, V., Thirion, B., Grisel, O., Blondel, M., Prettenhofer, P., Weiss, R., Dubourg, V., Vanderplas, J., Passos, A., Cournapeau, D., Brucher, M., Perrot, M., Duchesnay, E., 2011. Scikit-learn: Machine learning in Python. Journal of Machine Learning Research 12, 2825–2830.

Platias, C., Petasis, G., 2020. A Comparison of Machine Learning Methods for Data Imputation, in: 11th Hell. Conf. Artif. Intell., ACM. pp. 150–159. doi:10.1145/3411408.3411465.

Qin, C., Shi, B., Liao, R., Mansi, T., Rueckert, D., Kamen, A., 2019. Unsupervised Deformable Registration for Multi-modal Images via Disentangled Representations, in: Chung, A.C.S., Gee, J.C., Yushkevich, P.A., Bao, S. (Eds.), Inf. Process. Med. Imaging, Springer International Publishing, Cham. pp. 249–261.

Reuter, M., Schmansky, N.J., Rosas, H.D., Fischl, B., 2012. Within-subject template estimation for unbiased longitudinal image analysis. NeuroImage 61, 1402–1418. doi:10.1016/j.neuroimage.2012.02.084.

Rezende, D.J., Mohamed, S., Wierstra, D., 2014. Stochastic Backpropagation and Approximate Inference in Deep Generative Models .

Shi, Y., N, S., Paige, B., Torr, P., 2019. Variational Mixture-of-Experts Autoencoders for Multi-Modal Deep Generative Models, in: Wallach, H., Larochelle, H., Beygelzimer, A., d\textquotesingle Alché-Buc, F., Fox, E., Garnett, R. (Eds.), Adv. Neural Inf. Process. Syst. 32. Curran Associates, Inc., pp. 15718–15729.

Tabarestani, S., Aghili, M., Eslami, M., Cabrerizo, M., Barreto, A., Rishe, N., Curiel, R.E., Loewenstein, D., Duara, R., Adjouadi, M., 2020. A distributed multitask multimodal approach for the prediction of Alzheimer's disease in a longitudinal study. Neuroimage 206, 116317.

Tognin, S., van Hell, H.H., Merritt, K., Winter-van Rossum, I., Bossong, M.G., Kempton, M.J., Modinos, G., Fusar-Poli, P., Mechelli, A., Dazzan, P., Maat, A., de Haan, L., Crespo-Facorro, B., Glenthøj, B., Lawrie, S.M., McDonald, C., Gruber, O., van Amelsvoort, T., Arango, C., Kircher, T., Nelson, B., Galderisi, S., Bressan, R., Kwon, J.S., Weiser, M., Mizrahi, R., Sachs, G., Maatz, A., Kahn, R., McGuire, P., McGuire, P., Tognin, S., Fusar-Poli, P., Kempton, M., Modinos, G., Merritt, K., Mechelli, A., Dazzan, P., Gifford, G., Petros, N., Antoniades, M., De Micheli, A., Vieira, S., Spencer, T.J., Scarpazza, C., Hird, E., Kahn, R., Maat, A., van Hell, E., Winter, I., Cahn, W., Schnack, H., de Haan, L., Siegmann, D., Barkhof, J., Hendriks, L., de Wit, I., Crespo-Facorro, B., Tordesillas-Gutierrez, D., Setien-Suero, E., Ayesa-Arriola, R., Suarez-Pinilla, P., Ramirez-Bonilla, M., Garcia-de la foz, V.O., Glenthøj, B., Erlang Sørensen, M., Tangmose, K., Schæbel, H., Broberg, B., Rostrup, E., Lawrie, S., McDonald, C., Hallahan, B., Cannon, D., McLoughlin, J., Finnegan, M., Gruber, O., van Amelsvoort, T., Deckers, D., Marcelis, M., Vingerhoets, C., Arango, C., Díaz-Caneja, C.M., Ayora, M., Janssen, J., Rodríguez-Jiménez, R., Díaz-Marsá, M., Kircher, T., Falkenberg, I., Bitsch, F., Berger, P., Sommer, J., Raab, K., Jakobi, B., Nelson, B., McGorry, P., Amminger, P., McHugh, M., Galderisi, S., Mucci, A., Bucci, P., Piegari, G., Pietrafesa, D., Nicita, A., Patriarca, S., Bressan, R., Zugman, A., Gadelha, A., Rodrigues da Cunha, G., Soo Kwon, J., Kevin Cho, K.I.k., Young Lee, T., Kim, M., Bin Kwak, Y., Jeong Hwang, W., Weiser, M., Mizrahi, R., Kiang, M., Gerritsen, C., Maheandiran, M., Ahmed, S., Prce, I., Lepock, J., Sachs, G., Willeit, M., Lenczowski, M., Sauerzopf, U., Weidenauer, A., Furtner-Srajer, J., Kirschner, M., Maatz, A., Burrer, A., Stämpfli, P., Huber, N., Kaiser, S., Kawohl, W., Brammer, M., Young, J., Bullmore, E., Morgan, S., 2020. Towards Precision Medicine in Psychosis: Benefits and Challenges of Multimodal Multicenter Studies—PSYSCAN: Translating Neuroimaging Findings From Research into Clinical Practice. Schizophr. Bull. 46, 432–441. doi:10.1093/schbul/sbz067.

van Buuren, S., Groothuis-Oudshoorn, K., 2011. mice: Multivariate imputation by chained equations in r. Journal of Statistical Software 45, 1–67. URL: https://www.jstatsoft.org/v45/i03/.

Venugopalan, J., Tong, L., Hassanzadeh, H.R., Wang, M.D., 2021. Multimodal deep learning models for early detection of Alzheimer's disease stage. Sci. Rep. 11, 3254.

Vieira, S., Pinaya, W.H.L., Garcia-Dias, R., Mechelli, A., 2020. Multimodal integration, in: Mach. Learn. - Methods Appl. to Brain Disord.. Elsevier. chapter 16, pp. 283–305. doi:10.1016/B978-0-12-815739-8.00016-X.

Vincent, P., Larochelle, H., Bengio, Y., Manzagol, P.A., 2008. Extracting and composing robust features with denoising autoencoders, in: Proc. 25th Int. Conf. Mach. Learn. - ICML '08, ACM Press, New York, New York, USA. pp. 1096–1103. doi:10.1145/1390156.1390294.

Wang, S., Manning, C., 2013. Fast dropout training. Proc. 30th Int. Conf. Mach. Learn. 28, 118–126.

Wang, W., Arora, R., Livescu, K., Srebro, N., 2015. Stochastic optimization for deep CCA via nonlinear orthogonal iterations, in: 2015 53rd Annu. Allert. Conf. Commun. Control. Comput., IEEE. pp. 688–695.

Wei, W., Poirion, E., Bodini, B., Durrleman, S., Ayache, N., Stankoff, B., Colliot, O., 2019. Predicting PET-derived demyelination from multimodal MRI using sketcher-refiner adversarial training for multiple sclerosis. Med. Image Anal. 58. doi:10.1016/j.media.2019.101546.

Wei, W., Poirion, E., Bodini, B., Tonietto, M., Durrleman, S., Colliot, O., Stankoff, B., Ayache, N., 2020. Predicting PET-derived myelin content from multisequence MRI for individual longitudinal analysis in multiple sclerosis. Neuroimage 223, 117308.

Wu, M., Goodman, N., 2018. Multimodal Generative Models for Scalable Weakly-Supervised Learning, in: Bengio, S., Wallach, H., Larochelle, H., Grauman, K., Cesa-Bianchi, N., Garnett, R. (Eds.), Adv. Neural Inf. Process. Syst. 31. Curran Associates, Inc., pp. 5575–5585.

Yang, J., Li, X., Pak, D., Dvornek, N.C., Chapiro, J., Lin, M., Duncan, J.S., 2020. Cross-Modality Segmentation by Self-supervised Semantic Alignment in Disentangled Content Space, in: Albarqouni, S., Bakas, S., Kamnitsas, K., Cardoso, M.J., Landman, B., Li, W., Milletari, F., Rieke, N., Roth, H., Xu, D., Xu, Z. (Eds.), Domain Adapt. Represent. Transf. Distrib. Collab. Learn., Springer International Publishing, Cham. pp. 52–61.

Zhou, T., Fu, H., Chen, G., Shen, J., Shao, L., 2020. Hi-Net: Hybrid-Fusion Network for Multi-Modal MR Image Synthesis. IEEE Trans. Med. Imaging 39, 2772–2781. doi:10.1109/TMI.2020.2975344.

Zhou, T., Thung, K., Zhu, X., Shen, D., 2019. Effective feature learning and fusion of multimodality data using stage-wise deep neural network for dementia diagnosis. Hum. Brain Mapp. 40, 1001–1016.

Supplementary Material

S1. Derivation of the Lower Bound

The exact solution to the inference problem induced by Eq. (1) is given by the posterior $p\left(\mathbf{z}|\left\{\mathbf{x}_{d,n,v},\boldsymbol{\theta}_v\right\}_{v=1}^{V_{d,n}}\right)$, that is not generally computable analytically. Following Antelmi et al. (2019), we can nevertheless look for its approximation $q(\mathbf{z})$ through *Variational Inference* (Blei et al., 2017). By introducing the latent variational approximation $q(\mathbf{z})$, we can derive the lower bound on the marginal log-likelihood for a single data-point as follows:

$$\begin{aligned}\ln p\left(\mathbf{x}_{d,n,v}|\boldsymbol{\theta}_v\right) &= \ln \int p\left(\mathbf{x}_{d,n,v}|\mathbf{z},\boldsymbol{\theta}_v\right) p(\mathbf{z})\ d\mathbf{z} \\ &= \ln \int \frac{q(\mathbf{z})}{q(\mathbf{z})} p\left(\mathbf{x}_{d,n,v}|\mathbf{z},\boldsymbol{\theta}_v\right) p(\mathbf{z})\ d\mathbf{z} \\ &= \ln \mathbb{E}_{q(\mathbf{z})}\left[\frac{p\left(\mathbf{x}_{d,n,v}|\mathbf{z},\boldsymbol{\theta}_v\right) p(\mathbf{z})}{q(\mathbf{z})}\right] \\ &\geq \mathbb{E}_{q(\mathbf{z})}\left[\ln p\left(\mathbf{x}_{d,n,v}|\mathbf{z},\boldsymbol{\theta}_v\right)\right] - \mathcal{D}_{\mathrm{KL}}\left(q(\mathbf{z})\|p(\mathbf{z})\right).\end{aligned} \tag{S1}$$

To derive the last line of Eq. (S1) we leverage on the *Jensen's inequality* and collect the result into a new expectation term and in the Kullback-Leibler divergence term ($\mathcal{D}_{\mathrm{KL}}$).

We define the distribution function $q(\mathbf{z})$ to depend on a specific dataset d, data-point n, and view w, such that:

$$q(\mathbf{z}) = q_{d,n,w}(\mathbf{z}) = q\left(\mathbf{z}|\mathbf{x}_{d,n,w},\boldsymbol{\phi}_w\right), \tag{S2}$$

where $\boldsymbol{\phi}_w$ represents the view-specific variational parameters shared among all datasets. To force a link among views, we impose the inequality Eq. (S1) to hold for any w in $1\dots V_{d,n}$. To do so, we average the right hand side of Eq. (S1) across the $V_{d,n}$ views and rewrite Eq. (S1) as follows:

$$\ln p\left(\mathbf{x}_{d,n,v}|\boldsymbol{\theta}_v\right) \geq \mathcal{L}_v^{(\mathbf{x}_{d,n})} = \frac{1}{V_{d,n}} \sum_{w=1}^{V_{d,n}} \mathcal{L}_{w\to v}^{(\mathbf{x}_{d,n})}, \tag{S3}$$

where

$$\mathcal{L}_{w\to v}^{(\mathbf{x}_{d,n})} = \mathbb{E}_{q_{d,n,w}(\mathbf{z})}\left[\ln p\left(\mathbf{x}_{d,n,v}|\mathbf{z},\boldsymbol{\theta}_v\right)\right] - \mathcal{D}_{\mathrm{KL}}\left(q_{d,n,w}(\mathbf{z})\|p(\mathbf{z})\right) \tag{S4}$$

is the lower bound associated to the data-point $\mathbf{x}_{d,n}$ when its view v is predicted from its view w.

S2. Data Generation

Data points with V views $\mathbf{x}_{d,n} = \{\mathbf{x}_{d,n,v}\}_{v=1}^{V}$ with $\mathbf{x}_{d,n,v} \in \mathbb{R}^{f_v}$ where created from a common latent code $\mathbf{z}_{d,n} \in \mathbb{R}^l$ with l latent dimensions according to the following model:

$$\begin{aligned}&\mathbf{z}_{d,n} \sim \mathcal{N}(\mathbf{0};\mathbf{I}_l), \\ &\boldsymbol{\epsilon}_v \sim \mathcal{N}\left(\mathbf{0};\mathbf{I}_{f_v}\right), \\ &\mathbf{G}_v = diag\left(\mathbf{R}_v\mathbf{R}_v^T\right)^{-1/2}\mathbf{R}_v, \\ &\mathbf{x}_{d,n,v} = \mathbf{G}_v\mathbf{z}_{d,n} + \mathrm{SNR}^{-1/2}\cdot\boldsymbol{\epsilon}_v,\end{aligned} \tag{S5}$$

where for every view v, $\mathbf{R}_v \in \mathbb{R}^{f_v \times l}$ is a random matrix with l orthonormal columns (*i.e.,* $\mathbf{R}_v^T \mathbf{R}_v = \mathbf{I}_l$), $\mathbf{G}_v$ is the linear generative law, and SNR is the signal-to-noise ratio. With this choice, the diagonal elements of the covariance matrix of $\mathbf{x}_{d,n,v}$ are inversely proportional to SNR, *i.e.,* $diag\left(\mathbb{E}\left[\mathbf{x}_{d,n,v}\mathbf{x}_{d,n,v}^T\right]\right) = (1 + \text{SNR}^{-1})\mathbf{I}_{f_v}$. This generative Scenarios where generated by varying one-at-a-time the dataset attributes, as listed in Tab. S1.

Table S1: Dataset attributes, varied one-at-a-time in the prescribed ranges, and used to generate scenarios according to Eq. (S5).

Attribute description	Iteration list
Total views (V)	3 4 5
Features per view (f_v)	5 10 100
Latent space dimension (l)	2 4 8
Training Samples	100 500 1000
Testing Samples	1000
Signal-to-noise ratio (SNR)	1 3 10 100
Seed (re-initialize $\mathbf{R}_v$)	1 2 3 4 5